Growth of Quantum-Confined Indium Phosphide inside MCM-41

Jonathan R. Agger,[†] Michael W. Anderson,*,[†] Martyn E. Pemble,[†,§] Osamu Terasaki,[‡] and Yasuo Nozue[‡]

Department of Chemistry, UMIST, P.O. Box 88, Manchester M60 1QD, U.K., and Department of Physics, Tohoku University, Aramaki Aoba, Sendai 980, Japan

Received: September 12, 1997; In Final Form: December 23, 1997

An array of analytical techniques comprising powder X-ray diffraction, solid-state NMR spectroscopy, high-resolution transmission electron microscopy, nitrogen adsorption, and UV/vis diffuse reflectance spectroscopy has been applied to study the incorporation of indium phosphide semiconductor inside MCM-41 materials by metal organic chemical vapor deposition. Line broadening in the X-ray diffraction patterns suggests the existence of both large surface deposited indium phosphide particles and nanosized indium phosphide particles deposited within the pores. High-resolution transmission electron microscopy corroborates this result: surface deposits have been imaged, and analysis of electron diffraction patterns provides evidence of the existence of nanoparticles. Nitrogen adsorption provides information on pore filling. Quantum-confinement effects, brought about by the nanoparticle size regime, are evidenced by upfield shifting of the indium phosphide resonance in the ^{31}P magic-angle-spinning NMR spectra and by blue shifting of the band gap dependent transition in the UV/vis absorption spectra.

Introduction

In recent years, it has become increasingly clear that major breakthroughs in electronic systems technology will come from devices with optoelectronic properties governed by low dimensionality. Interest in the field was first sparked in 1981 when Ekimov and Onushchenko[1] discovered significant differences between the absorption spectra of small copper chloride particles and those of the bulk material. Éfros and Éfros[2] explained this phenomenon as being due to three-dimensional space quantization of an exciton, which may lead to the following effects: blue shifting of the semiconductor band gap;[1,2] increase in the third-order, Kerr optical susceptibility,[3] leading to enhanced nonlinear optical properties; and increase in the oscillator strength for exciton radiative recombination,[4] leading to fast optical response.

The remarkable nature of such quantum size effects and their possible uses in a new generation of optoelectronic devices has led to a wealth of research into their production and characterization. As one-dimensional, quantum well, electron confinement is already a well-established technology, research has concentrated on the production of two-dimensionally-confined quantum wires and three-dimensionally-confined quantum dots. There are two conceivable routes for the production of such minute structures: the first involves etching the desired topology from a larger initial structure; the second involves some form of self-limiting organization as the structure is assembled from scratch.

Due to limited resolution and excitonic quenching at etch-damaged boundaries, the first route has met with only limited success.[5] Many different synthetic approaches have been employed to bring about the self-limiting organization upon which the second route depends. These include colloid technology,[6] doping of polymer matrixes,[7] and the use of serpentine superlattices.[8] However, perhaps the most intuitively elegant method yet conceived for creating semiconductor self-limiting organization is that of using porous materials as hosts. Early work concentrated exclusively on the use of zeolitic materials due to their optical transparency in the visible and near UV region and the great variety of regular, well-defined pore structures available.[9] Three main synthetic pathways toward the incorporation of semiconductor into such materials have been attempted: vapor phase transport;[10] cation exchange followed by either thermal treatment or treatment with a gaseous group V or VI hydride;[11] and metal–organic chemical vapor deposition (MOCVD).[12]

The major problem in employing zeolite hosts is the inevitable dominance of the host–guest interface on the optoelectronic performance of the semiconductor, due to the micropore size regime (2–20 Å). The discovery of the M41S family of materials[13] allows access to the mesopore size range (20–100 Å), thus offering a possible solution to this problem. Filling of the two-dimensional, hexagonal array of uniform mesopores of MCM-41 with semiconductor should result in an ordered array of quantum wires.

In this paper we present the first inclusion of the direct band gap III–V semiconductor, indium phosphide, within the pores of MCM-41. One of the aims is to demonstrate how conventional solid-state characterization techniques can be usefully employed in conjunction with optical measurements to gain a better understanding of these new heterostructures.

Experimental Section

Materials for MCM-41 Synthesis. Silica sources were CAB-O-SIL M5 fumed silica, BDH Merck, and tetraethyl orthosilicate, Aldrich. The quaternary ammonium surfactant salts ($C_nH_{2n+1}(CH_3)_3NX$, X = Cl or Br) were obtained from Lancaster, Aldrich, and Kodak, either in the solid form or as a

---

† UMIST.
§ Current address: Department of Chemistry, University of Salford, Salford M5 4WT, U.K.
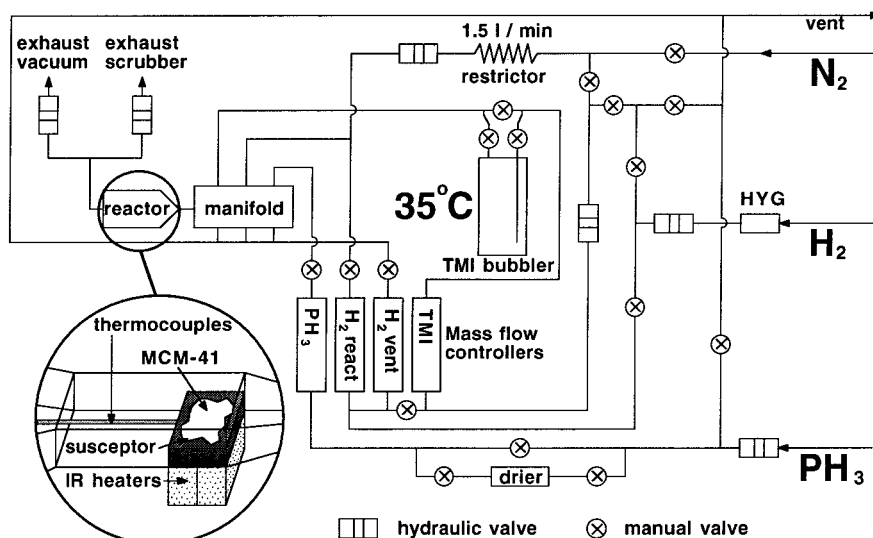‡ Tohoku University.

Figure 1. Simplified plan of the MOCVD reactor used in this study, showing gas inlets, gas mass flow controllers, reactor manifold, and glass reactor.

25 wt % solution. The tetrabutylammonium hydroxide used was supplied by Janssen. All chemicals were used as received.

Materials for the Metal–Organic Chemical Vapor Deposition. The solid trimethylindium was obtained from Epichem Ltd., and all gases used, i.e., air, phosphine, N_2, and H_2, were supplied by the British Oxygen Company.

Metal–Organic Chemical Vapor Deposition Equipment. All semiconductor growth reported in this work was carried out in a continuous flow MOCVD reactor supplied by British Telecom. Figure 1 is a simplified diagram of this reactor showing hydrogen, nitrogen, and phosphine inlets, various gas mass-flow controllers, the trimethylindium bubbler, the reactor manifold, and the reactor itself. During reaction and purging, all exhaust gases were vented to an Ecoguard 1000 Mimic scrubber unit.

Instrumentation. Powder X-ray diffraction data were obtained on a Scintag XDS 2000 diffractometer in continuous scan mode using Cu Kα_1 radiation and an energy dispersive detector. Two different sets of source and detector slits were used: for low-angle scanning (2θ in the range $1-10°$) source slits of 0.5 and 1 mm and detector slits of 0.3 and 0.2 mm were used, and for all other scans (2θ out to $80°$) source slits of 2 and 4 mm and detector slits of 0.5 and 0.3 mm were used. ^{29}Si and ^{31}P magic-angle-spinning (MAS) NMR spectra were recorded on a Bruker MSL 400 solid-state spectrometer. ^{29}Si spectra were recorded at 79.494 MHz using 7 mm zirconia rotors, spinning at ca. 4 kHz and 6 μs, 90° pulses with a 720 s interpulse delay, and ca. 80 transients. ^{31}P spectra were recorded at 161.977 MHz using 4 mm zirconia rotors, spinning at ca. 10 kHz and 6 μs, 90° pulses with a 15 s interpulse delay with high-power proton decoupling, and ca. 5000 transients. Tetramethylsilane (TMS) and phosphoric acid were used respectively as external chemical shift standards. Nitrogen sorption data were obtained using a computer-controlled gravimetric balance. Samples were dehydrated by heating at 450 °C under vacuum to constant weight. Nitrogen adsorption isotherms were then measured at 77 K allowing 30 min to reach steady weight before recording each data point. UV/vis diffuse reflectance spectra were recorded using a tungsten lamp, a monochromator with three different diffraction gratings, a silicon photodiode, and a Hamamatu R636-10 photomultiplier. Samples were sealed in 10 mm diameter UV transparent quartz tubes under 100 mmHg of helium gas, which served as an inert atmosphere to conduct

TABLE 1: Preparation of Surfactant Solutions

preparation	form of surfactant	mass of surfactant[a] (g)	mass of water[b] (g)
C_{16} MCM-41	25% wt aq sol chloride	17.90	4.48
C_{14} MCM-41	solid bromide	4.62	18.48
C_{12} MCM-41	solid chloride	3.62	14.48

[a] Each surfactant quantity represents 0.014 mol of surfactant: Surfactant/silica mole ratio = 0.14. [b] Water was adjusted to make each surfactant 20% wt in water.

heat away from the sample during analysis. Normal reflectance from the glass tube was eliminated by having an oblique angle of incidence of the light. The standard sample used to normalize the reflectance data was a synthetic, white zeolite powder. These normalized reflectance data were then converted to absorption data by application of the Kubelka–Munk function. High-resolution transmission electron microscopy (HRTEM) images and electron diffraction patterns were obtained on a JEOL 4000 EX operating at 400 kV. Z-contrast microscopy was performed on a VG601-UX field emission gun scanning transmission electron microscope (STEM).

Synthesis. Purely siliceous MCM-41 materials of varying pore diameter were synthesized using surfactants with different carbon chain lengths. These materials are henceforth designated by the length of this carbon chain. For example, C_{16} MCM-41 was synthesized using hexadecyltrimethylammonium halide. As all the gels, regardless of liquid crystal used, were prepared with equivalent reagent mole ratios, only the preparation of C_{16} MCM-41 is given. Table 1 shows the quantity and kind of liquid crystal used in each synthesis.

A. Synthesis of C_{16} MCM-41 Using $C_{16}H_{33}(CH_3)_3N$ Cl. Water (4.48 g) was added to 17.90 g of $C_{16}H_{33}(CH_3)_3N$ Cl solution (25 wt %) to form a 20 wt % solution. To this was added 8.25 g of tetrabutylammonium hydroxide solution (40 wt %) and 3.75 g of tetraethyl orthosilicate (98%+). The resulting mixture was well stirred both prior to and during the addition of 5.00 g of fumed silica. This gel was then placed in a static polyethylene bottle at 95 °C for 48 h. After cooling to room temperature, the resulting solid product was recovered by vacuum filtration, extensively washed with water, and dried in air at room temperature. The powder X-ray diffraction pattern of the as-synthesized material exhibits four reflections, characteristic of high-quality MCM-41, having *d* spacings which index to *hk*0 two-dimensional hexagonal ordering. The *d*
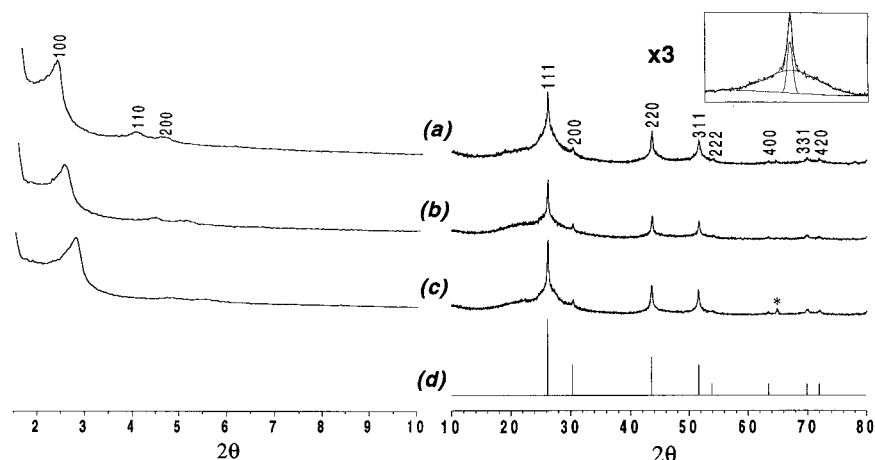
Indium Phosphide inside MCM-41

J. Phys. Chem. B, Vol. 102, No. 18, 1998 **3347**

Figure 2. Powder X-ray diffraction patterns of (a) C_{16} MCM-41, (b) C_{14} MCM-41 and (c) C_{12} MCM-41, all infilled with indium phosphide, and (d) the indium phosphide JCPDS pattern. The high-angle region of the scans has been expanded three times. The reflection marked with an asterisk is due to the aluminum sample holder. Inset is a deconvolution of the InP (111) reflection of the C_{12} MCM-41 sample.

spacing of the high-intensity (100) reflection was 41.3 Å, corresponding to a pore repeat distance, a_0, of 47.7 Å calculated from $a_0 = 2d_{100}/\sqrt{3}$. The as-synthesized material was then calcined in flowing air for 12 h at 540 °C. Powder X-ray diffraction of the resulting material reveals the disappearance of the (210) reflection while the remaining reflections are shifted to lower d spacing; for example, the d spacing of the (100) reflection decreases to 37.9 Å, corresponding to a pore repeat distance a_0 of 43.8 Å. This slight lattice contraction after calcination of ca. 4 Å has been documented previously.[13b]

B. MOCVD Growth of InP inside C_{16} MCM-41. A 2 g sample of the calcined C_{16} MCM-41 was placed in the reactor and dehydrated overnight at 400 °C under 200 cm³ min⁻¹ clean, dry, flowing nitrogen. The reactor temperature was then reduced to 52 °C and the thermostat on the trimethylindium bubbler was set to 35 °C. The nitrogen flow was replaced by hydrogen: 200 cm³ min⁻¹ direct to the reactor; 500 cm³ min⁻¹ to vent; 60 cm³ min⁻¹ to the reactor via the trimethylindium bubbler. The hydrogen flow through the trimethylindium bubbler was stopped after a period of 4 h. The reactor temperature was quickly increased to 300 °C, and a flow of 20 cm³ min⁻¹ of phosphine gas was admitted. Although the phosphine treatment was of 3 h duration to try to minimize diffusion effects, the sample color started to darken within a minute and had reached its final dark brown color within 5 min. The quantities of trimethylindium and phosphine used may be calculated from eqs 1 and 2:

$$TMIn_{mol\,flux} = \frac{flow\,rate \times p_{TMIn}}{V_m p},$$

$$\log p_{TMIn} = B - A/T_{bubbler} \quad (1)$$

where $B = 10.52$ and $A = 3014$ K

$$PH_{3\,mol\,flux} = \frac{flow\,rate}{V_m} \quad (2)$$

where p_{TMIn} is the partial pressure in mmHg of trimethylindium in the reactor, V_m is the molar volume, p is the total pressure (760 mmHg), and A and B are standard constants. In this work, 4.6×10^{-3} mol of trimethylindium were supplied over a 4 h period and 0.16 mol of phosphine over a 3 h period. The phosphine was thus in large excess. After treatment, the reactor was flushed with nitrogen at room temperature before being opened to the atmosphere. The samples thus produced showed

TABLE 2: d-Spacings (Å) of the Major Reflections in the Powder X-ray Diffraction Patterns for As-Synthesized, Calcined, and Infilled MCM-41 Samples

C_{16} MCM-41				C_{14} MCM-41				C_{12} MCM-41			
d_{100}	d_{110}	d_{200}	d_{210}	d_{100}	d_{110}	d_{200}	d_{210}	d_{100}	d_{110}	d_{200}	d_{210}
As-Synthesized											
41.3	24.0	20.9	15.8	36.5	21.2	18.5	14.0	34.0	19.9	17.2	13.0
Calcined											
38.0	21.7	18.9		33.4	19.6	16.9		30.8	18.0	15.5	
InP Infilled											
38.7	22.1	19.4		35.5	20.2	17.5		31.7	18.3	15.9	

no sensitivity to atmospheric moisture over a time period in excess of six months.

Results

Powder X-ray Diffraction. Three main features can be seen in the powder X-ray diffraction patterns of the infilled materials shown in Figure 2a−c. First, the highly ordered pore structure is still intact after the growth process, evidenced by the low-angle region $2\theta = 1-10°$. Inclusion of the semiconductor results in a small increase in the pore repeat. Values of d spacings for the major reflections in the as-synthesized, calcined, and semiconductor infilled samples are given in Table 2. Second, the amorphous nature of the silicate host material matrix gives rise to a very broad reflection centered at ca. $2\theta = 24°$. Third, reflections characteristic of indium phosphide can be seen in the patterns out to $2\theta = 80°$, as evidenced by the joint crystallographic powder diffraction standard (JCPDS) pattern shown in Figure 2d. A good fit of the indium phosphide (111) reflections at ca. $2\theta = 26°$ was achieved using two Gaussian peak profiles per reflection with very different full widths at half-maximum (fwhm), as is shown in the inset of Figure 2. Using the fwhm for the same reflection in a pattern obtained from a powdered indium phosphide single-crystal wafer as a reference, the Scherrer formula, enabled calculation of the particle sizes for the two composite peak profiles. The narrower peak profiles all yielded average crystallite sizes of ca. 480 Å, which varied little for samples with different pore diameter. The broader peak profiles yielded average crystallite sizes of 43, 41, and 34 Å for C_{16}, C_{14}, and C_{12} samples, respectively. These data suggest two kinds of indium phosphide crystallites: large surface-deposited particles of constant size and much smaller particles which are most probably within the pores and hence show a size correlated to the pore diameter of the host material.
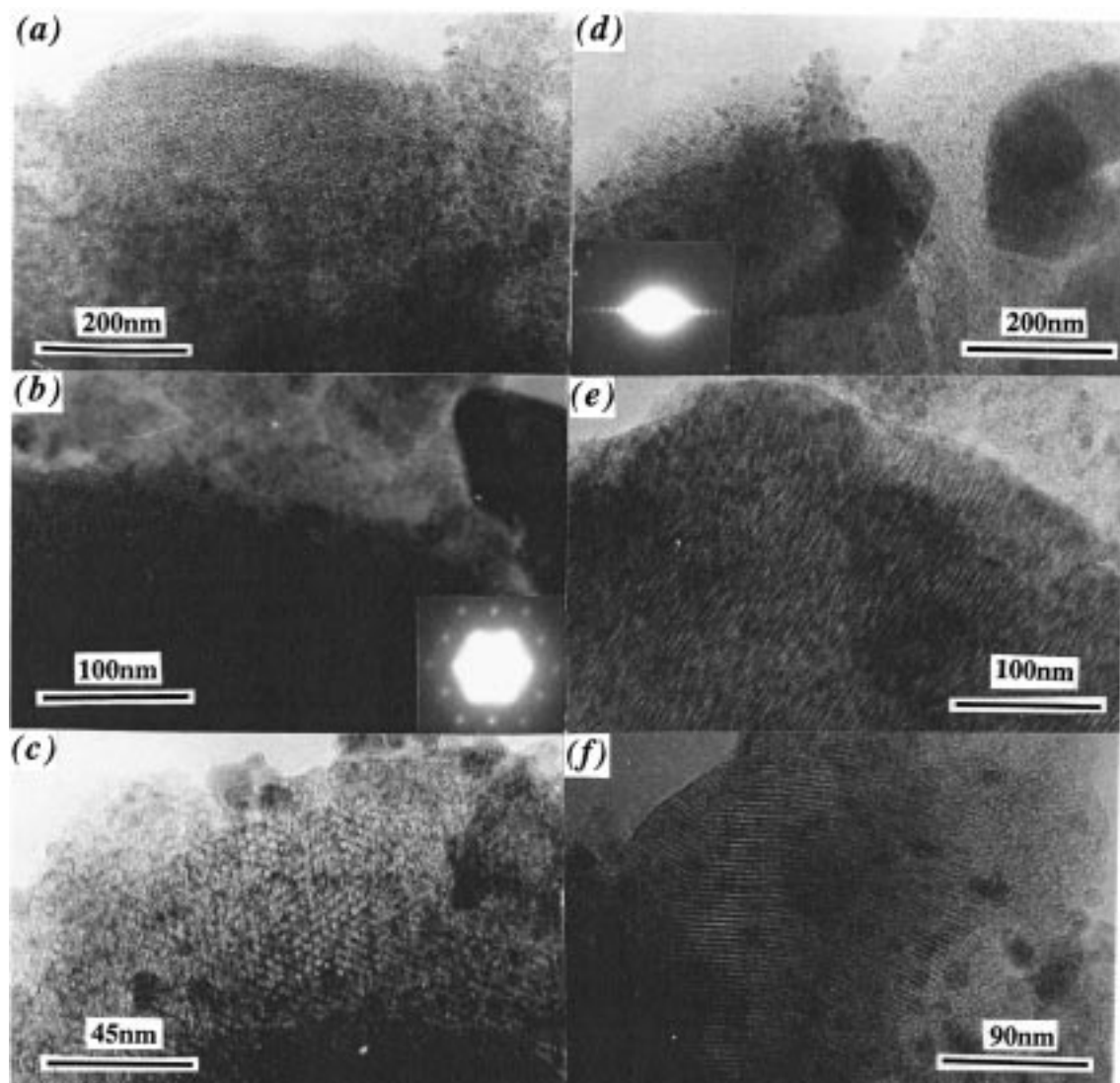
Figure 3. TEM micrographs, taken with the beam direction parallel (a), (b), and (c) and perpendicular (d), (e), and (f) to the pore direction, of C_{16} MCM-41, C_{14} MCM-41, and C_{12} MCM-41 infilled with indium phosphide, respectively. Insets in (b) and (d) are the electron diffraction patterns from which the images were produced.

These results highlight the presence of indium phosphide particles with sizes on the order of pore dimensions.

High-Resolution Transmission Electron Microscopy, Electron Diffraction, and Z-Contrast Microscopy. Further evidence that the highly ordered host material pore structure has been preserved during the semiconductor growth process is provided by transmission electron micrographs of infilled C_{16}, C_{14}, and C_{12} samples shown in Figure 3a–f. In the micrographs taken with the beam direction parallel to the pore direction, Figure 3a–c, the hexagonally ordered pore structure can clearly be seen despite many dark areas, which are probably surface deposits of indium phosphide. Presence of the latter supports the powder X-ray diffraction data, which suggests the existence of large crystallites. Figure 3b shows in the inset the electron diffraction (ED) pattern from which the image was formed. This pattern shows a hexagonal array of diffraction spots brought about by the two-dimensional hexagonal ordering of the pores perpendicular to the beam direction. Figure 3d–f shows micrographs taken with the beam direction perpendicular to the pores. Again, both ordered pore structure and large surface deposits of indium phosphide are evident. Figure 3d shows in the inset the electron diffraction pattern from which the image was formed. This pattern shows a line of very bright, closely

spaced spots. The fact that the spots appear as a line and not in some other pattern of higher symmetry indicates one-dimensional order perpendicular to the beam direction, which is the case for MCM-41. The pattern is typical of that expected for the host material in every respect but one: the intensity of the spots. This leads to the conclusion that indium atoms, being the heaviest scattering atoms present, must also exist in an ordered array imposed by the host material.

Since the ordering of the indium atoms within the pores is brought about by the host material, it therefore follows that the periodicity of this ordering should match the periodicity of the ordered host. The very narrow spacing between the spots is indicative of order having a repeat distance in the mesopore range. The calculated periodicity of 21.6 Å compares well with the C_{16} MCM-41 d_{110} spacing of the host material, shown in Figure 4, of 22.1 Å. The diffraction spots observed in this electron diffraction pattern are therefore due to the {110} planes.[14] The excellent match between the periodicity of arrayed indium atoms and the periodicity of the host matrix indicates that the ordering of indium atoms has been dictated by the host structure. Since this is only possible if a large proportion of indium atoms are incorporated within the pore structure, this
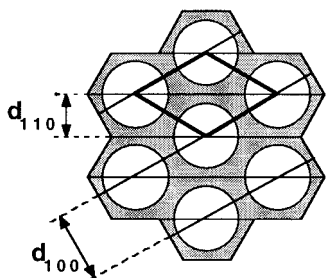
Indium Phosphide inside MCM-41

J. Phys. Chem. B, Vol. 102, No. 18, 1998 **3349**

Figure 4. Cross-sectional view of MCM-41 looking along [001].

result provides evidence that the semiconductor material has been confined within the pores.

A Z-contrast microscopy bright-field image of an indium phosphide infilled C_{16} MCM-41 sample, Figure 5a, shows the ordered hexagonal pore structure with surface deposits, which appear as dark regions. The brightness of these deposits in the dark-field image, Figure 5b, shows that they contain indium. More interestingly, smaller bright dots can also be seen. The brightness indicates that these dots also contain In, and the size is on the order of a cross-sectional pore area. These images provide further evidence of the incorporation of indium phosphide within the pores of MCM-41.

^{29}Si and ^{31}P MAS NMR Studies. In a siliceous MCM-41 material, assuming that Q^4 silicon atoms are more likely to exist in the wall interior and Q^3 silicon atoms at the pore wall interface, it follows that accurate deconvolution of ^{29}Si MAS NMR spectra may help to elucidate the wall structure of these materials. A long recycle delay of 720 s was employed in the recording of all ^{29}Si MAS NMR spectra of MCM-41 materials in the present study in order allow full relaxation of all silicon environments.[15]

^{29}Si MAS NMR spectra of the uncalcined samples exhibit two broad, well-resolved resonances at ca. -100 and -110 ppm corresponding to Q^3 and Q^4 silicons, respectively. The Q^3/Q^4 ratio varies little with changing pore size, as can be seen from the data in Table 3. The greater number of Q^4 silicons compared to Q^3 silicons implies that the wall structure of MCM-41 is more complicated than simply walls comprising internal Q^4 silicons lined with pore/wall interface Q^3 silicons.

Upon calcination of the samples there is a distinct broadening of the two resonances, making accurate deconvolution difficult. However, there is a significant decrease in the Q^3/Q^4 ratio, as shown in Table 3, owing to some condensation of neighboring Q^3 silicons. Spectra of the indium phosphide infilled materials exhibit a further slight broadening of the two resonances. This is manifest in the greater error associated with the deconvolution data, though within this error there appears to be little change in the Q^3/Q^4 ratio and hence the wall structure of the material.

^{31}P MAS NMR spectra, shown in Figure 6, were recorded to elucidate the nature of the semiconductor within the pores. The isotropic chemical shift value of -143.9 ppm obtained for ^{31}P in bulk indium phosphide, Figure 6d, is in good agreement with previously published values.[16] The large line width of ca. 7 kHz is probably due to isotropic, indirect coupling to indium atoms with possibly a small contribution from incompletely averaged, direct, dipolar coupling (N.B. the latter interaction will be isotropic in view of the tetrahedral phosphorus environment). Each spectrum of an infilled sample, Figure 6a−c, shows two features: first, a peak around 0 ppm attributed to phosphate, spinning sidebands of which are marked with asterisks; second, a series of unresolved peaks shifted upfield from -143.9 ppm, assigned to indium phosphide. This upfield broadening must, for a spin half nucleus, be due to heterogeneity in the indium
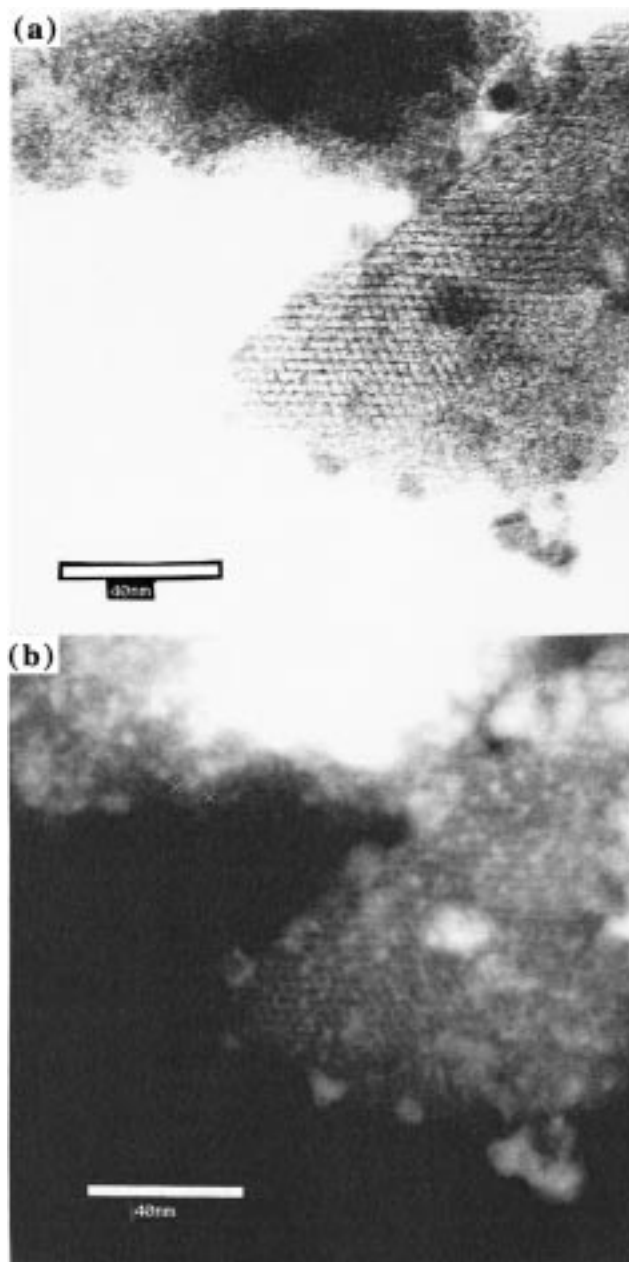

Figure 5. Z-contrast microscopy images of an indium phosphide infilled C_{16} MCM-41 sample: (a) bright-field and (b) dark-field.

phosphide chemical shift. Two possibilities exist: (i) heterogeneity in the diamagnetic shielding due to a range of chemical environments near the semiconductor/host material interface;[17] (ii) heterogeneity in the paramagnetic shielding due to quantum confinement effects, which are discussed below. While, relative to the bulk material, a paramagnetic effect will always produce a net upfield shift (as observed experimentally), a diamagnetic shift could be either upfield or downfield dependent upon shielding. We therefore consider the ^{31}P MAS NMR spectra to be good evidence for quantum confinement.

For a cubic, binary semiconductor, the downfield paramagnetic contribution to chemical shift σ_p is given by[18]

$$\sigma_p = \left(\frac{\mu_0 e^2 \hbar^2}{4\pi m_e^2}\right) \Delta U^{-1} \langle r^{-3} \rangle (1 - \alpha^2) \qquad (3)$$

where σ_p arises from the residual angular momentum of excited electrons with p-character that are mixed into the electronic

TABLE 3: ^{29}Si MAS NMR Deconvolution Data

	uncalcined				calcined				InP infilled			
	Q^3		Q^4		Q^3		Q^4		Q^3		Q^4	
sample	δ/ppm	%	δ/ppm	%	δ/ppm	%	δ/ppm	%	δ/ppm	%	δ/ppm	%
C_{16} MCM-41	−100.4	33	−111.1	67	−100.2	12	−109.1	88	−100.1	18	−110.8	82
C_{14} MCM-41	−99.3	34	−110.3	66	−101.4	15	−110.1	85	−100.2	8	−109.9	92
C_{12} MCM-41	−99.9	35	−110.2	65	−99.9	14	−109.0	86	−100.9	26	−109.3	74
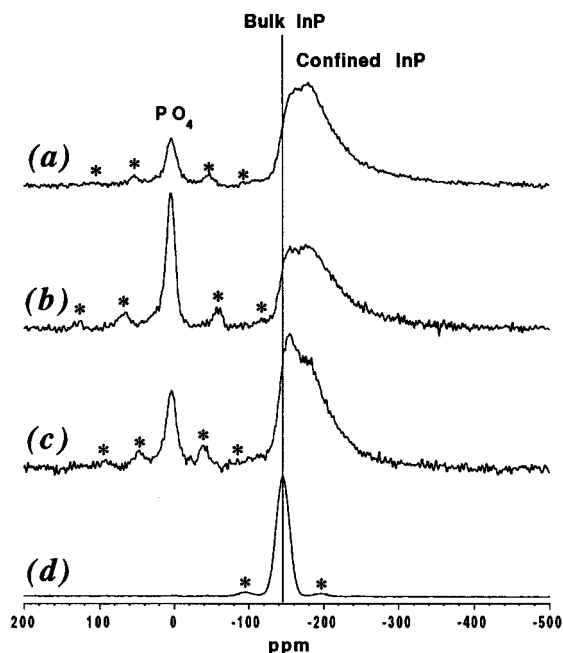
Figure 6. Comparative ^{31}P MAS NMR spectra of (a) C_{16} MCM-41, (b) C_{14} MCM-41, and (c) C_{12} MCM-41 infilled with indium phosphide and (d) powdered indium phosphide single-crystal wafer. Spinning sidebands are marked with asterisks.

ground state by covalency effects. ΔU is the average excitation energy which specifies how far away in energy these excited electronic states are, $\langle r^{-3} \rangle$ is the expectation value of the distance of p electrons from the nucleus, and α is the Phillips ionicity, a measure of the bond covalency. Other constants have their usual meanings. It is the parameter ΔU that is thought to be most sensitive to size quantization effects. An increase in the average excitation energy, brought about by an increase in the semiconductor band gap, caused by quantum confinement, will decrease the paramagnetic contribution to the chemical shift and hence result in an upfield displacement of the resonance.

Nitrogen Adsorption Measurements. Nitrogen adsorption isotherms, shown in Figure 7, were recorded at 77 K to try to glean information on the porosity of the calcined and indium phosphide infilled materials. The isotherms are type IV in the Brunauer, Deming, and Deming and Teller (BDDT) classification, characteristic of adsorption in mesopores. However, somewhat unusually, they are all reversible; that is, within experimental error there is an absence of hysteresis between the adsorption and desorption branches of the isotherm. Hysteresis is usually associated with capillary condensation/evaporation. Complete reversibility in nitrogen adsorption isotherms recorded at 77 K on MCM-41 has been reported by Branton et al.[19] as being due to instability of the nitrogen meniscus. Multilayer adsorption on the surface is the most likely alternative.

Despite their unusual reversible nature, it is still possible to glean much information from these nitrogen adsorption isotherms and other related plots. Table 4 lists the main parameters calculated from the data. The BET monolayer capacities, n_m-

(BET), and the BET constants, c(BET), are calculated from the slopes and intercepts of the BET plots in the usual manner. Values of the mesopore volume V_p have been calculated from the volumes of nitrogen adsorbed for the final readings of the adsorption branch by assuming that the pores have filled with liquid adsorptive. The density of liquid nitrogen at 77 K has been taken as 0.808 g cm^{-3}.[20] The BET internal surface areas, A(BET), have been calculated from the BET monolayer capacities, assuming the nitrogen molecular area, a_m, to be 0.162 nm^2 in the completed monolayer.[21] Values for the pore diameter d^p have been calculated from the Kelvin equation and corrected for the multilayer thickness t. In addition to the mean pore diameters calculated from values of p/p^0 at step inflection points, also included in Table 4 are the maximum and minimum pore diameters calculated from values of p/p^0 at the beginning and end of the steps.

The isotherms for the calcined samples prior to growth, Figure 7a−c, show a reduction in pore volume from C_{16} MCM-41 to C_{14} MCM-41, though there is no further reduction for C_{12} MCM-41. C_{14} MCM-41 has the smallest internal surface area. The pore diameters show a decrease from C_{16} MCM-41 down to C_{12} MCM-41, as expected. Subtraction of the maximum and minimum pore diameters, d^p, from the pore repeat distances, a_0, yields ranges of possible wall thickness of 10.6 to 18.1 Å, 9.4 to 17.4 Å, and 10.1 to 17.5 Å for C_{16}, C_{14}, and C_{12} MCM-41, respectively. These ranges may be considered as being constant within experimental error. Nitrogen adsorption data on nonporous hydroxylated silica[22] have been used to construct α_s plots in which the amount of gas adsorbed is plotted against α_s, the reduced standard adsorption at the corresponding p/p^0 (with $\alpha_s = 1$ at $p/p^0 = 0.4$). The fact that the initial linear region of these plots can be extrapolated back to the origin confirms the absence of any detectable micropore filling at low relative pressure p/p^0. The deviation from linearity present at higher p/p^0 values is an indication of the onset of mesopore filling.

The nitrogen adsorption isotherms of the semiconductor-infilled MCM-41 materials, shown in Figure 7d−f, are of exactly the same nature as the isotherms of the calcined hosts prior to growth. Table 5 lists the main parameters that have been calculated from the data in exactly the same manner as for the isotherms of the hosts prior to growth. Again, the fact that the initial linear region of the α_s plots can be extrapolated back to the origin confirms the absence of any detectable micropore filling at low relative pressure p/p^0, and the deviation from linearity present at higher p/p^0 values is an indication of the onset of mesopore filling.

Comparing the data in Tables 4 and 5, the C_{16} MCM-41 sample shows a decrease in pore volume of 37% and a corresponding decrease in internal surface area of 41% after semiconductor growth. Filling of the C_{14} MCM-41 sample has occurred to a lesser extent, causing a 30% decrease in pore volume and a 27% decrease in internal surface area. The C_{12} MCM-41 sample shows a 34% decrease in pore volume and a 30% decrease in internal surface area. These results indicate that pore filling by the semiconductor is incomplete. Also, the
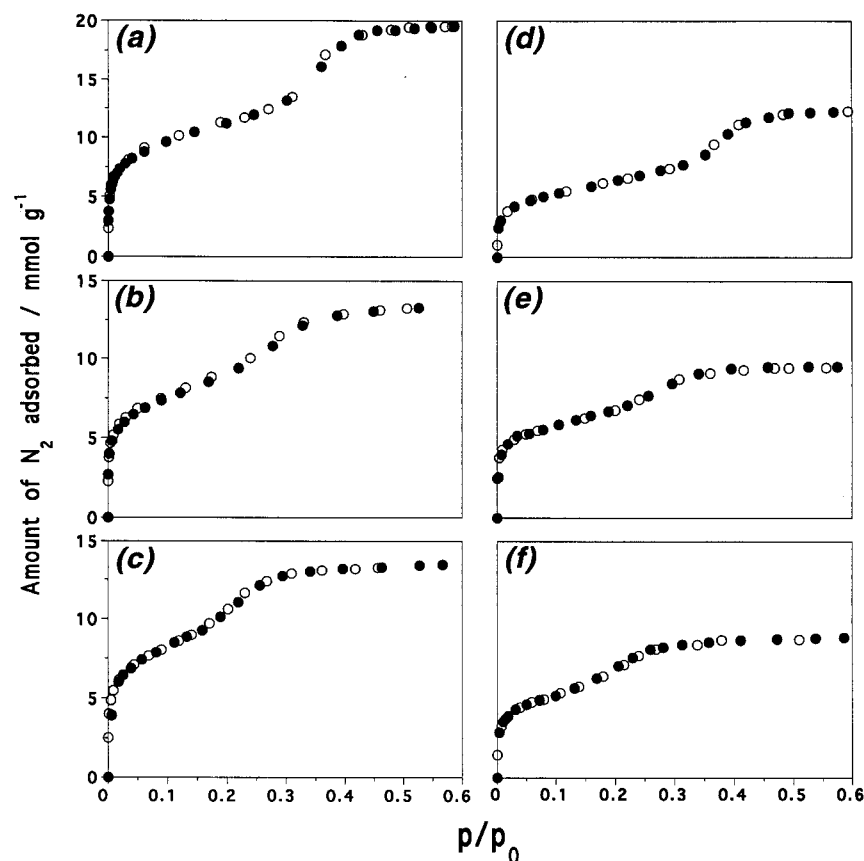
Figure 7. Nitrogen adsorption isotherms recorded at 77 K of (a) C_{16} MCM-41, (b) C_{14} MCM-41, and (c) C_{12} MCM-41 calcined samples and (d) C_{16} MCM-41, (e) C_{14} MCM-41, and (f) C_{12} MCM-41 infilled with indium phosphide.

TABLE 4: Adsorption of Nitrogen on Calcined MCM-41 at 77 K

sample	n_m(BET)/ mmol g^{-1}	c(BET)	A(BET)/ m^2 g^{-1}	V_p/ cm^3 g^{-1}	d^p_{min}/ Å	d^p_{max}/ Å	d^p_{mean}/ Å
C_{16} MCM-41	9.09	282	887	0.68	25.8	33.3	28.7
C_{14} MCM-41	7.64	131	745	0.47	21.2	29.2	25.9
C_{12} MCM-41	9.09	60	887	0.47	18.1	25.5	22.0

TABLE 5: Adsorption of Nitrogen on Indium Phosphide Infilled MCM-41 at 77 K

sample	n_m(BET)/ mmol g^{-1}	c(BET)	A(BET)/ m^2 g^{-1}	V_p/ cm^3 g^{-1}	d^p_{min}/ Å	d^p_{max}/ Å	d^p_{mean}/ Å
C_{16} MCM-41	5.32	120	519	0.43	27.0	36.7	29.3
C_{14} MCM-41	5.59	109	545	0.33	21.2	28.7	24.3
C_{12} MCM-41	6.32	87	617	0.31	18.6	24.9	21.4

decreases in both internal surface area and pore volume are not accompanied by any significant change in the mean pore diameter. Changes of +0.6, −1.6, and −0.6 Å are observed for C_{16}, C_{14}, and C_{12} MCM-41, respectively, going from the unfilled to the filled sample. Within experimental error, these can all be considered as negligible. This implies that the indium phosphide does not line the internal pore surface, as this would be accompanied by a drop in pore diameter of at least 4 Å. With the likelihood of the trimethylindium precursor reacting with silanol groups and thus effectively coating the internal surface of the host material, the following mechanism for semiconductor deposition is proposed. The trimethylindium precursor diffuses into the pore void, where it reacts with the abundant silanol groups on the pore surface. Methane gas is liberated as the metal−organic anchors itself to the host material in the form of dimethylindium or monomethylindium species.[23] After removal of any excess metal−organic by flushing with hydrogen, subsequent diffusion of an excess of the phosphine

precursor into the pores results in reaction with the anchored species to form indium phosphide, with the liberation of yet more methane and regeneration of the silanol groups. The newly formed indium phosphide then agglomerates within the pores, resulting in the observed constant pore radius and decrease in both internal surface area and pore volume. In view of the excess phosphine precursor and the signals for phosphate observed in the ^{31}P MAS NMR spectra, these wires might be anchored via phosphate linkages.

Subtraction of the maximum and minimum pore diameters, d^p, from the pore repeat distances, a_0, yields ranges of possible wall thickness of 8.0 to 17.7 Å, 12.3 to 19.8 Å, and 11.7 to 18.0 Å for C_{16}, C_{14}, and C_{12} MCM-41, respectively. These ranges are similar in magnitude to those calculated for the bare, calcined host materials and may again be considered as being constant within experimental error. This indicates that deposition of semiconductor within the pores does not significantly perturb the silicate wall structure.

UV/Vis Diffuse Reflectance Spectroscopy. The UV/vis absorption spectra of the three indium phosphide infilled samples, shown in Figure 8a−c, have been obtained by applying the Kubelka−Munk function to diffuse reflectance spectra. The general shape of all three spectra is typical of bulk indium phosphide, being an absorption continuum with onset around 1.3 eV.[24] Although the shoulders, denoted by asterisks, represent optical transitions within the materials, their energies may not easily be gleaned from this figure. Hence Figure 8d−f shows the first derivative of the absorption coefficients shown in Figure 8a−c. In these spectra, the absorption bands may be discerned.

In the range 1−4 eV a pair of doublets are observed in the spectrum of bulk indium phosphide.[25] Spectra of the infilled
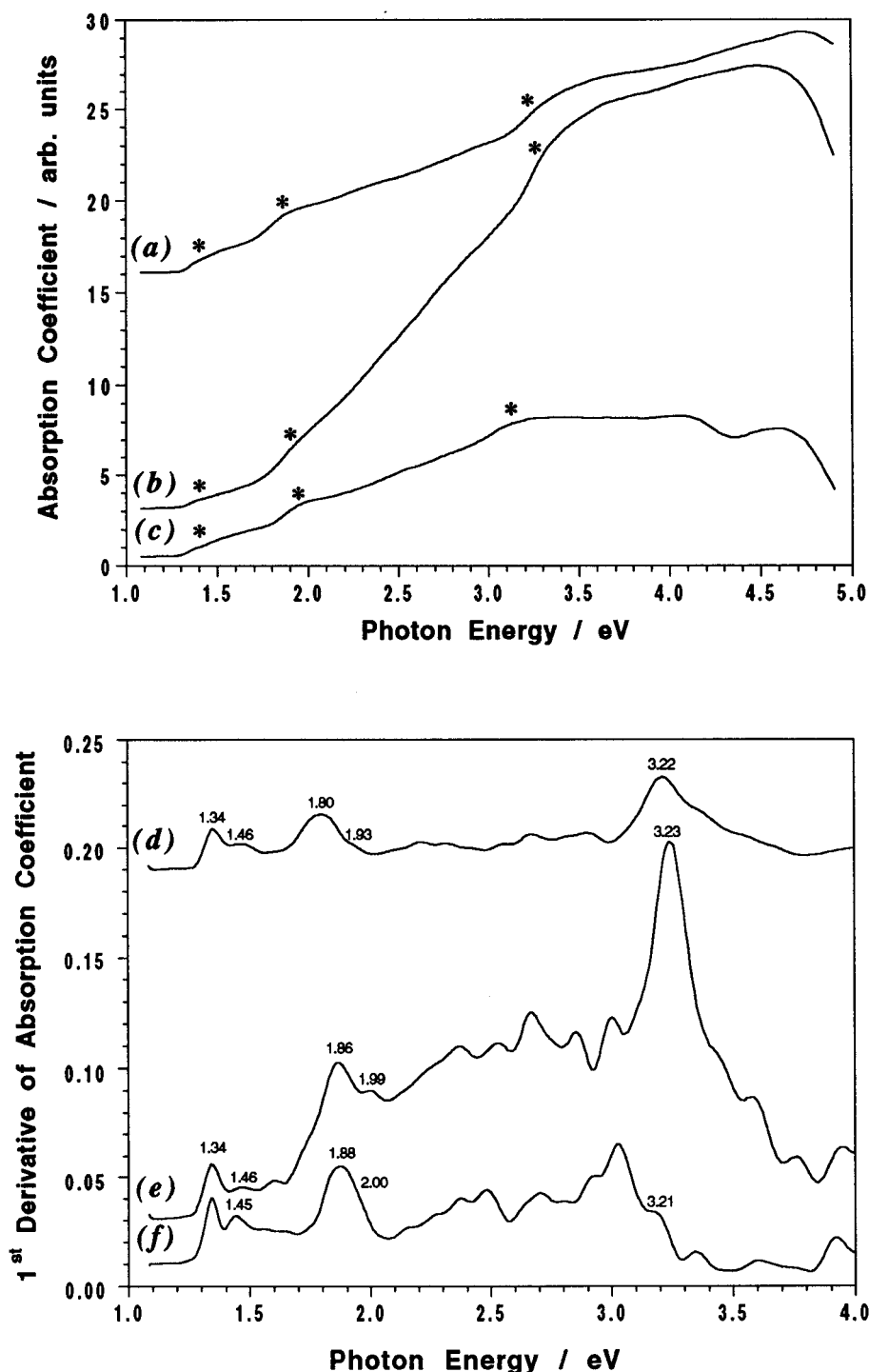
Figure 8. UV/vis absorption spectra, recorded at room temperature, of (a) C_{16} MCM-41, (b) C_{14} MCM-41, and (c) C_{12} MCM-41 infilled with indium phosphide. (d), (e), and (f) show the first derivatives of (a), (b), and (c), respectively.

MCM-41 samples show a clear doublet at around 1.34 and 1.46 eV assigned to the band gap dependent E_0, $E_0+\Delta_0$ transitions. The splitting of ca. 0.11 eV agrees well with a previously published value of 0.1 eV.[26] The band at ca. 3.2 eV is assigned to the E_1 and $E_1+\Delta_1$ transitions. It is not possible to see the Δ_1 splitting, though this may well be an artifact of recording the spectra at room temperature. The energy of this band at around 3.2 eV also agrees well with previously published work.[26] The existence of these two bands supports the presence of bulk indium phosphide deposits which have been seen in the TEM images and which show up in the powder XRD patterns as narrow reflections.

However, the band at around 1.9 eV is a feature not seen in the spectrum of the bulk material. The magnitude of the splitting of this doublet of 0.12 eV is very similar to the magnitude of the splitting of the band gap characteristic E_0, $E_0+\Delta_0$ doublet of 0.11 eV. The other interesting feature is the correlation between host material pore size and energy of this doublet. For C_{16} MCM-41 it appears at 1.80 and 1.93 eV, while in the C_{14} MCM-41 sample it is blue-shifted to 1.86 and 1.99 eV, and in the C_{12} MCM-41 sample it is further blue-shifted to 1.88 and 2.00 eV. This doublet may therefore be attributed to the E_0, $E_0+\Delta_0$ transitions occurring in indium phosphide deposited within the pores. This blue shifting of the band gap

Indium Phosphide inside MCM-41

J. Phys. Chem. B, Vol. 102, No. 18, 1998 **3353**

dependent transition is typically characteristic of quantum confinement of the semiconductor brought about by the restricted pore size.

Conclusions

In this work we have used a combination of techniques to confirm both inclusion and quantum confinement of InP within the pore system of MCM-41. Powder X-ray diffraction serves to highlight both the ordered pore structure of the host materials before and after the growth process and ultimately the presence of indium phosphide, deposited both within the pores and on the surface. Although the broad nature of the signals observed in the ^{29}Si MAS NMR spectra precluded a detailed analysis of the host material wall structure, it has been demonstrated that ^{31}P MAS NMR can be usefully employed to detect quantum-confinement effects. Nitrogen adsorption isotherms and their related BET and α_s plots provide a wealth of information concerning the pore volume, internal surface area and pore diameter of host materials both before and after growth. In conjunction with powder XRD data these results allow an estimate of wall thickness. The use of an unambiguous structural technique such as transmission electron microscopy yields much information on both pore structure and semiconductor deposition both on the surface and within the pores.

It is our belief that in view of the very nature of heterogeneous semiconductor infilled porous host materials, evidence for quantum-confinement effects in such materials should not be sought purely on the basis of optical measurements, which can be very difficult to interpret due to the semiconductor−host interface and general broadness of the bands observed. For this reason, the work presented in this study encompasses a wide variety of analytical techniques, all of which contribute to the overall picture.

References and Notes

(1) Ekimov, A. I.; Onushchenko, A. A. *Sov. Phys. Semicond.* **1982**, *16*, 775.

(2) Éfros, Al. L.; Éfros, A. L. *Sov. Phys. Semicond.* **1982**, *16*, 772.

(3) (a) Horan, P.; Blau, W. *Z. Phys. D: At., Mol. Clusters* **1989**, *12*, 501. (b) Roussignol, P.; Ricard, D.; Flytzanis, C. *Proc. SPIE-Int. Soc. Opt. Eng.* **1989**, *1017*, 20.

(4) (a) Matsuura, M.; Kamizato, T. *Surf. Sci.* **1986**, *174*, 183. (b) Kayanuma, Y. *Phys. Rev. B* **1991**, *44*, 13085.

(5) (a) Broers, A. N. *Nanostructure Physics and Fabrication*; Academic Press: New York, 1989; p 421. (b) Sotomayor Torres, C. M.; Watt, M.; Arnot, H. E. G.; Glew, R.; Crusco Cornet, R.; Kerr, T. M.; Beaumont, S. P. *Surf. Sci.* **1990**, *228*, 275.

(6) (a) Brus, L. E. *J. Phys. Chem.* **1986**, *90*, 2555. (b) Nedeljkovic, J. M.; Nenadovic, M. T.; Micic, O. I.; Nozik, A. J. *J. Phys. Chem.* **1986**, *90*, 12. (c) Nozik, A. J.; Williams, F.; Nenadovic, M. T.; Rajh, T.; Micic, O. I. *J. Phys. Chem.* **1985**, *89*, 397. (d) Eychmüller, A.; Hässelbarth, A.; Weller, H. *J. Lumin.* **1992**, *53*, 113. (e) Eychmüller, A.; Hässelbarth, A.; Katsikas, L.; Weller, H. *J. Lumin.* **1991**, *48, 49*, 745. (f) Steigerwald, M. L.; Brus, L. E. *Annu. Rev. Mater. Sci.* **1989**, *19*, 471. (g) Herron, N.; Wang, Y.; Eckert, H. *J. Am. Chem. Soc.* **1990**, *112*, 1322.

(7) (a) Wang, Y.; Herron, N. *Chem. Phys. Lett.* **1992**, *200*, 71. (b) Wang, Y.; Herron, N.; Mahler, W.; Suna, A. *J. Opt. Soc. Am. B* **1989**, *6*, 808.

(8) Miller, M. S.; Weman, H.; Pryor, C. E.; Krishnamurthy, M.; Petroff, P. M.; Kroemer, H.; Merz, J. L. *Phys. Rev. Lett.* **1992**, *68*, 3464.

(9) Breck, D. W. *Zeolite Molecular Sieves*; Wiley & Sons: New York, London, Sydney, Toronto, 1988.

(10) (a) Terasaki, O.; Yamazaki, K.; Thomas, J. M.; Oshuna, T.; Watanabe, D.; Sanders, J. V.; Barry, J. C. *Nature* **1987**, *330*, 58. (b) Parise, J. B.; MacDougall, J. E.; Herron, N.; Farlee, R.; Sleight, A. W.; Wang, Y.; Bein, T.; Moller, K.; Moroney, L. M. *Inorg. Chem.* **1988**, *27*, 221. (c) Dag, O.; Kuperman, A.; Ozin, G. A. *Adv. Mater.* **1994**, *6*, 147. (d) Terasaki, O. *Acta Chem. Scand.* **1991**, *45*, 785. (e) Tang, Z. K.; Nozue, Y.; Goto, T. *J. Phys. Soc. Jpn.* **1992**, *61*, 2943.

(11) (a) Uchida, H.; Ogata, T.; Yoneyama, H. *Chem. Phys. Lett.* **1990**, *173*, 103. (b) Liu, X.; Iu, K.-K.; Thomas, J. K. *Chem. Phys. Lett.* **1992**, *195*, 163. (c) Stramel, R. D.; Nakamura, T.; Thomas, J. K. *J. Chem. Soc., Faraday Trans. 1* **1988**, *84*, 1287. (d) Liu, X.; Thomas, J. K. *Langmuir* **1989**, *5*, 58. (e) Sun, T.; Seff, K. *J. Phys. Chem.* **1993**, *97*, 7719. (f) Wang, Y.; Herron, N. *J. Phys. Chem.* **1987**, *91*, 257. (g) Moller, K.; Eddy, M. M.; Stucky, G. D.; Herron, N.; Bein, T. *J. Am. Chem. Soc.* **1989**, *111*, 2564. (h) Herron, N.; Wang, Y.; Eddy, M. M.; Stucky, G. D.; Cox, D. E.; Moller, K.; Bein, T. *J. Am. Chem. Soc.* **1989**, *111*, 530. (i) Wark, M.; Schulz-Ekloff, G.; Jaeger, N. I.; Lutz, W. *Mater. Res. Soc. Symp. Proc.* **1991**, *233*, 133.

(12) (a) Steele, M. R.; MacDonald, P. M.; Ozin, G. A. *J. Am. Chem. Soc.* **1993**, *115*, 7285. (b) Ozin, G. A.; Steele, M. R. *Adv. Mater.* **1994**, *6*, 300. (c) MacDougall, J. E.; Eckert, H.; Stucky, G. D.; Herron, N.; Wang, Y.; Moller, K.; Bein, T.; Cox, D. *J. Am. Chem. Soc.* **1989**, *111*, 8007.

(13) (a) Kresge, C. T.; Leonowicz, M. E.; Roth, W. J.; Vartuli, J. C.; Beck, J. S. *Nature* **1992**, *359*, 710. (b) Beck, J. S.; Vartuli, J. C.; Roth, W. J.; Leonowicz, M. E.; Kresge, C. T.; Schmitt, K. D.; Chu, C. T.-W.; Olson, D. H.; Sheppard, E. W.; McCullen, S. B.; Higgins, J. B.; Schlenker, J. L. *J. Am. Chem. Soc.* **1992**, *114*, 10834.

(14) Leon, R.; Margolese, D.; Stucky, G. D.; Petroff, P. M. *Phys. Rev. B* **1995**, *52*, R2285.

(15) Steel, A.; Carr, S. W.; Anderson, M. W. *Chem. Mater.* **1995**, *7*, 1829.

(16) Duncan, T. M.; Karlicek, R. F.; Bonner, A. A.; Thiel, F. A. *J. Phys. Chem. Solids* **1984**, *45*, 389.

(17) Potter, L. D.; Guzelian, A. A.; Alivisatos, A. P.; Wu, Y. *J. Chem. Phys.* **1995**, *103*, 4834.

(18) (a) Ramsey, N. F. *Phys. Rev.* **1950**, *78*, 699. (b) Eckert, H.; Yesinowski, J. P. *J. Am. Chem. Soc.* **1986**, *108*, 2140.

(19) Branton, P. J.; Hall, P. G.; Sing, K. S. W.; Reichert, H.; Schüth, F.; Unger, K. K. *J. Chem. Soc., Faraday Trans.* **1994**, *90*, 2965.

(20) *Handbook of Chemistry and Physics*; CRC Press Inc.: Boca Raton, FL, 1986; p B-26.

(21) Sing, K. S. W.; Everett, D. H.; Haul, R. A. W.; Moscou, L.; Pierotti, R. A.; Rouquérol, J.; Siemieniewska, T. *Pure Appl. Chem.* **1985**, *57*, 603.

(22) Bhambhani, M. R.; Cutting, P. A.; Sing, K. S. W.; Turk, D. H. *J. Colloid Interface Sci.* **1972**, *38*, 109.

(23) Anderson, M. W.; Logothetis, G. K.; Pemble, M. E.; Taylor, A. G.; Wallace, N. C.; Yates, H. M. *Adv. Mater. Opt. Electron.* **1993**, *2*, 313.

(24) Rinnen, K. D.; Kolenbrander, K. D.; DeSantolo, A. M.; Mandich, M. L. *J. Phys. Chem.* **1992**, *96*, 4088.

(25) Cardona, M.; Shaklee, K. L.; Pollak, F. H. *Phys. Rev.* **1967**, *154*, 696.

(26) Matatagui, E.; Thompson, A. G.; Cardona, M. *Phys. Rev.* **1968**, *176*, 950.